

SHS synthesis, SPS densification and mechanical properties of nanometric tungsten

Sarah Dine, Elodie Bernard, Nathalie Herlin, Christian Grisolia, David Tingaud, Dominique Vrel

▶ **To cite this version:**

Sarah Dine, Elodie Bernard, Nathalie Herlin, Christian Grisolia, David Tingaud, et al.. SHS synthesis, SPS densification and mechanical properties of nanometric tungsten. Metals, 2021, 11, pp.252. 10.3390/met11020252 . cea-03142396

HAL Id: cea-03142396

https://cea.hal.science/cea-03142396

Submitted on 16 Feb 2021

HAL is a multi-disciplinary open access archive for the deposit and dissemination of scientific research documents, whether they are published or not. The documents may come from teaching and research institutions in France or abroad, or from public or private research centers.

L'archive ouverte pluridisciplinaire **HAL**, est destinée au dépôt et à la diffusion de documents scientifiques de niveau recherche, publiés ou non, émanant des établissements d'enseignement et de recherche français ou étrangers, des laboratoires publics ou privés.



Distributed under a Creative Commons Attribution 4.0 International License

metals

MDPI

Article

SHS Synthesis, SPS Densification and Mechanical Properties of Nanometric Tungsten

Sarah Dine [1], Elodie Bernard [2], Nathalie Herlin [3], Christian Grisolia [2], David Tingaud [1] and Dominique Vrel [1,*]

[1] Laboratoire des Sciences des Procédés et des Matériaux (LSPM), Université Sorbonne Paris Nord, UPR 3407 CNRS, 93430 Villetaneuse, France; sarah.dine@lspm.cnrs.fr (S.D.); david.tingaud@lspm.cnrs.fr (D.T.)
[2] CEA, Institut de Recherche sur la Fusion par Confinement Magnétique (IRFM), 13108 Saint Paul lez Durance, France; Elodie.BERNARD@cea.fr (E.B.); Christian.GRISOLIA@cea.fr (C.G.)
[3] CEA, Institut Rayonnement Matière de Saclay (IRAMIS) UMR Nanosciences et Innovation pour les Matériaux, la Biomédecine et l'Énergie (NIMBE), Université Paris Saclay, 91191 Gif-sur-Yvette, France; nathalie.herlin@cea.fr
* Correspondence: dominique.vrel@lspm.cnrs.fr; Tel.: +33-1-4940-3411

Abstract: Recent studies have shown that low grain sizes are favorable to improve ductility and machinability in tungsten, as well as a resistance to ablation and spallation, which are key properties for the use of this material in a thermonuclear fusion environment (Tokamaks such as ITER). However, as one of the possible incidents during Tokamak operation is the leakage of air or water from the cooling system inside the chamber, resulting in the so-called loss of vacuum accident (LOVA), extensive oxidation may arise on tungsten components, and the use of an alloy with improved oxidation resistance is therefore highly desirable. As current production routes are not suitable for the fabrication of bulk nanostructured tungsten or tungsten alloys samples, we have proposed a new methodology based on powder metallurgy, including the powder synthesis, the densification procedure, and preliminary mechanical testing, which was successfully applied to pure tungsten. A similar study is hereby presented on tungsten-chromium alloys with up to 6 wt.% Cr. Results show that full tungsten densification may be obtained by SPS at a temperature lower than 1600 °C. The resulting morphology strongly depends on the amount of the alloying element, presenting a possible second phase of chromium oxide, but always keeps a partial nanostructure inherited from the synthesized powders. Such microstructure had previously been identified as being favorable to the use of these materials in fusion environments and for improved mechanical properties, including hardness, yield strength and ductility, all of which is confirmed by the present study.

Keywords: tungsten alloys; ductility; nanostructure; mechanical properties

check for updates

Citation: Dine, S.; Bernard, E.; Herlin, N.; Grisolia, C.; Tingaud, D.; Vrel, D. SHS Synthesis, SPS Densification and Mechanical Properties of Nanometric Tungsten. *Metals* **2021**, *11*, 252. https://doi.org/10.3390/met11020252

Academic Editor: Javier S. Blázquez Gámez
Received: 2 December 2020
Accepted: 30 January 2021
Published: 2 February 2021

Publisher's Note: MDPI stays neutral with regard to jurisdictional claims in published maps and institutional affiliations.

Copyright: © 2021 by the authors. Licensee MDPI, Basel, Switzerland. This article is an open access article distributed under the terms and conditions of the Creative Commons Attribution (CC BY) license (https://creativecommons.org/licenses/by/4.0/).

1. Introduction

Tungsten has been chosen as one of the principal candidates for plasma-facing components (PFC) in the construction of thermonuclear fusion tokamaks [1–6]. Indeed, among all the pure elements, it has the highest melting point while presenting a good thermal conductivity, which makes it interesting for any high-temperature application. Moreover, considering the specific conditions in tokamaks, it also presents a low activation under neutronic irradiation and low plasma sputtering. However, tungsten presents a strong drawback at room temperature for any structural application, as it is usually brittle. As a function of the preparation method used, and specifically of the presence of some impurities which may coalesce at grain boundaries [7], tungsten usually exhibit a ductile-to-brittle-transition-temperature (DBTT) within the 200–400 °C range. Indeed, due to this brittleness, cracking may pre-exist before operation due to machining, but more important, thermal cycling of PFC may also favor their formation and thus drastically reduce their life span [8,9].

In order to induce and improve ductility in tungsten, different pathways are currently being considered [6]. While in metallurgy, the use of alloying elements is usually the first solution investigated to improve one specific property in metal, this problem is hard to circumvent for tungsten ductility, as only rhenium (Re) has such a capacity [10]. This costly element is unfortunately inadequate for the construction of large-scale pieces such as in ITER plasma-facing components, and especially because in the specific operational conditions of thermonuclear fusion, with high neutron bombardment, rhenium is transmuted into long half-life radioactive osmium, inducing waste management and safety issues [11,12]. For similar reasons, the use of niobium and molybdenum should be avoided [13]. Neutron-induced embrittlement, reducing thermal conductivity, is also a strong drawback for which these elements should not be considered.

With these considerations in mind, the list of acceptable alloying elements in tungsten is reduced to only a few, including Ta, V, Cr, Ti, Si [14–19]. Among these possible alloying elements, Cr should be specifically mentioned for its possible contribution to the improvement of tungsten oxidation resistance [20–23]. It is indeed well-known that chromium has a natural tendency to form a thin protective oxide layer that passivates the material, which is the basic principle of its use in stainless steel.

However, tungsten wires in old-fashioned light bulbs are ductile enough to be shaped as small spirals, and this is due to the fine microstructure of the material resulting from the extrusion process used to produce these wires. Unfortunately, due to the high-temperature reached during the light bulb operation, recrystallization occurs, and this ductility is lost. To avoid or limit this phenomenon, some studies have investigated the addition of dispersed phases, such as La_2O_3, Y_2O_3, CeO_2 [6,24,25], TiC [26,27], ZrC [28] or HfC [11]. As these phases are insoluble in W, they precipitate at the grain boundaries and thus limit grain growth. As a result, the overall tungsten ductility after thermal cycling is improved, and the machinability may be preserved. Although these oxides and carbides are thermodynamically stable, their use in plasma-facing components that will be subjected to erosion should be considered cautiously. Indeed, the potential release of oxygen or carbon in the hydrogen plasma would result in detrimental pollution, with the possible formation of water or hydrocarbons. In addition, some of the metals in these compounds may form metal hydrides, resulting in large tritium retention.

For larger samples, obtaining these fine microstructures is more complex and may require processes such as equal channel angular pressing [29,30], cold rolling [31–33], surface attrition [34], or even high-pressure torsion [35]. Due to the high forces required in these processes, and the high elastic limit of tungsten, they are unfortunately not appropriate in order to obtain nanostructured plasma-facing components as large as the design of the ITER tokamak requires. Using these fine microstructures, recent investigations have shown that the DBTT can be reduced to a value as low as 77 K [31].

The use of chromium as a possible alloying element in tungsten, studied here mainly as a possible solution to increase tungsten oxidation resistance, has been previously investigated by other authors. It has been reported that the synthesis of dense W-Cr alloys is difficult due to low interdiffusion coefficients in this system [36] and that the use of a third element such as Pd would be necessary to improve interdiffusion [36–38]. However, the presence of palladium dissolves rather large amounts of tungsten and chromium, making the whole system more complex [39]. Moreover, the existence of a relatively low Cr-Pd eutectic may have a detrimental effect on the high-temperature properties of the resulting material [38,40], especially because this phase has been shown to form at grain boundaries [41]. Nanometric W-Cr alloys were also synthesized using high-energy milling from micrometric powders [22,42]. This technique, however, needing long milling times, implies a high level of energy consumption and leads inevitably to the contamination of the powders from the milling media.

2. Materials and Methods

In our previous works on pure W [43] and MoNbW alloys [44,45], we developed a new methodology to synthesize refractory metals nanopowders using self-propagating high-temperature synthesis (SHS). To preserve the nanostructure after densification, these powders were sintered by spark plasma sintering (SPS) [46], which allows a full or nearly full densification in short times. A similar study is conducted here on W-Cr alloys, with up to 6 wt.% Cr. Samples will be characterized using XRD (Equinox 1000 diffractometer, Cu kα_1 radiation, INEL, Artenay, France), SEM observations for the powders and the densified samples (ZEISS FEG-SEM Supra 40VP, Oberkochen, Germany), and these characterizations will also include electron backscattered diffraction (EBSD), and mechanical testing will be performed (hardness and compressive tests, DURAMIN 20 apparatus, STRUERS, Ballerup, Denmark) for the latter.

2.1. Nanopowders Synthesis

The powders were synthesized using the self-propagating high-temperature synthesis process, using the reduction of metal oxides by magnesium in thermite-like reactions, according to the protocol described in [43–45]. WO_3 (Alfa Aesar (Thermo Fisher GmbH, Kandel, Germany), 99.8%, ref. 11828 batch Q12F015), Cr_2O_3 (Alfa Aesar, 99.8%, ref. 12285 batch D26Z027), Mg (Sigma-Aldrich (Merck KGaA, Darmstadt, Germany), 97.9%, ref. 8.18506.500 batch S7714006-901) and NaCl (VWR (Avantor, Radnor, PA, USA), 100%, ref. 27800.360 batch 17C144128), acting, respectively as an oxidizer, reducer, and moderator were first carefully weighted in order to retrieve a 20 g final mass of alloy with 2, 4 or 6 wt.% of Cr (respectively mentioned to hereunder as WCr2, WCr4 and WCr6, Table 1), then thoroughly mixed in the powder form using a 3D Turbula mixer (WAB, Muttenz, Switzerland) for 24 h, and placed in a sealed reactor, surrounded by NaCl, before the following thermitic reaction was started by Joule-heating a tungsten wire placed at the bottom of the sample:

$$WO_3 + x\ Cr_2O_3 + (3 + 3x + y)\ Mg \rightarrow W + 2x\ Cr + 3\ MgO + y\ Mg$$

SEM micrographs of the reactants are presented in Figure 1. In order to make sure that the reaction is complete, 50% excess Mg was added from the stoichiometric proportions. As for NaCl, its introduction provides an increase of the global heat capacity of the mixture, and its amount was calculated to decrease the overall product's final temperature to 1800 °C. However, as the placement of a thermocouple proved to be difficult considering the temperatures reached, and as pyrometric measurements were not an option in our pressure sealed reactor, no temperature measurements were performed. The value of 1800 °C should therefore be considered as an estimate, allowing us to synthesize all our different samples in similar conditions. On the other hand, the introduction of NaCl in the SHS reaction is known to favor nanometric grain sizes in the resulting powders [43–45]. As magnesium has a low boiling point, these reactions were performed under confinement, for most of the gaseous magnesium to stay available for the reaction. For reference, the WCr2 experiment was also performed without confinement.

Table 1. Weighing of the reactants for the synthesis of 20 g of the different alloys. WCr2, WCr4 and WCr6 stand for 2, 4 and 6 weight percent chromium in the resulting tungsten alloy.

Alloy	Cr wt.%	Cr at.%	WO_3 (g)	Cr_2O_3 (g)	Mg (g)	NaCl (g)
WCr2	2	6.73	24.717	0.585	12.082	16.13
WCr4	4	12.84	24.213	1.169	12.264	15.76
WCr6	6	18.41	23.708	1.754	12.447	15.39

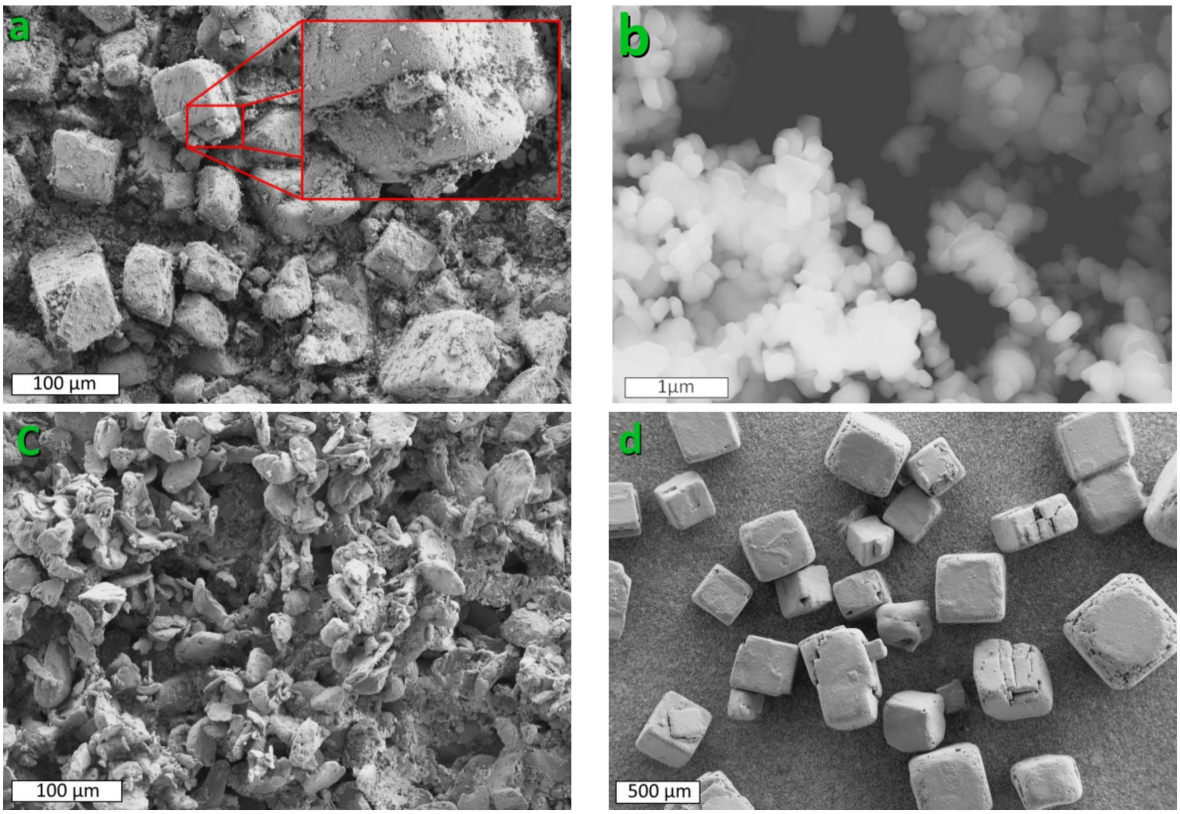


Figure 1. SEM observations of the reactants: (**a**) WO_3; (**b**) Cr_2O_3; (**c**) Mg; (**d**) NaCl. Note that tungsten trioxide particles seem to be made of large grains covered with submicronic particles (insert).

As the reaction scheme yields to the presence of MgO, residual Mg, and NaCl in the final powder mixture, these were lixiviated using 2 N hydrochloric acid for 2 h under stirring at 80 °C. The powders were then retrieved using a 0.22 µm polyethersulfone membrane filtration (MB Express Millipore®, MERCK, Damrstadt, Germany). To ensure complete dissolution of the contaminants, this procedure was performed twice, and the retrieved powders were then rinsed before a last filtration, and finally dried in an autoclave at 50 °C for 24 h. A similar reaction was previously investigated to synthesize stoichiometric W-Cr alloys [47] using aluminum as a reducer and without a reaction moderator. However, in this case, the separation between molten alumina and the molten alloy is performed using a high gravity field, inducing a composition gradient within the alloy.

After these steps are completed, the crystal structure of the obtained powders was analyzed using X-ray diffraction. This characterization was then followed by Rietveld refinement using the Materials analysis using diffraction (MAUD) software to determine the lattice parameters of the different alloys.

2.2. SPS Densification

Spark plasma sintering (SPS) was performed in the "plateforme IdF de frittage flash" (Thiais, France), on a Syntec 515 S machine (Fuji Electronic Industrial Co., Ltd., Saitama, Japan). ~5 g of the as-synthesized powders were inserted in graphite mold with a 10 mm diameter. The temperature is followed with an infrared pyrometer pointing to a hole allowing temperature measurement in the direct vicinity of the sample; consequently, temperature measurements were not possible under 600 °C. Pressure and piston movement measurements were also recorded, providing all the necessary information to analyze the different steps of the sintering.

Densification experiments were performed at 1600, 1800 and 2000 °C with a plateau time of 1 to 15 min. Most cycles were made of a single ramp with a heating rate of 50 °C·min^{-1}. However, to minimize the risk of a possible overshoot, the temperature

ramp is set to 20 °C·min^{-1} when the temperature is less than 50 °C under the maximum temperature. Some more complex temperature cycles were also tested, but with no significant differences in the final density and will not be presented. The compaction pressure is always 100 MPa, set at the beginning of the heating cycle, a pre-compaction at 42 MPa being set before. This pressure is released during the quenching of the sample.

2.3. Densified Samples

Densified samples were polished with 68 µm, 9 µm and 3 µm cloths (P220—Struers MD-Piano 220; P2400—Struers MD-Allegro; and P4000—Struers MD-Dac, respectively, STRUERS, Ballerup, Denmark), with an OPS finishing (colloidal silica, 40 nm—Struers MD-Chem). Densities have then been measured using Archimedes' method in orthoxylene.

Bulk samples were analyzed using X-ray diffraction then by Rietveld refinement. SEM observations were conducted, together with EDX local analysis and mapping. Grain sizes, preferential orientations and nature of grain boundaries were analyzed using electron backscattered diffraction (EBSD).

As for mechanical properties, Vickers hardness was measured on the plane perpendicular to the densification pressing direction using a 1.96 N force applied for 10 s. In order to increase the statistical precision of the measure, this measure was repeated 10 times on each sample. Due to the small sizes of the samples (10 mm diameter and 3–4 mm in thickness), we were unable to cut tensile test specimens. Instead, compression tests were performed on parallelepiped samples cut by electro-erosion, with dimensions 2.4 × 2.4 × 5.0 mm^3, by pressing along the main axis of the sample.

3. Results and Discussion

3.1. Nanopowders Synthesis

SEM observations, Figure 2, reveal mostly rounded particle shapes, with a large polydispersity, typically ranging from 10 to 200 nm. However, in some areas, particles seem bounded together as if local melting had occurred during the reaction, whatever the composition. This morphology is significantly different from what had been obtained with pure W [46], where particle shapes were mostly in the form of platelets. Moreover, we can observe that, while keeping a wide size distribution, the average particle size seems to decrease when the amount of Cr is increased.

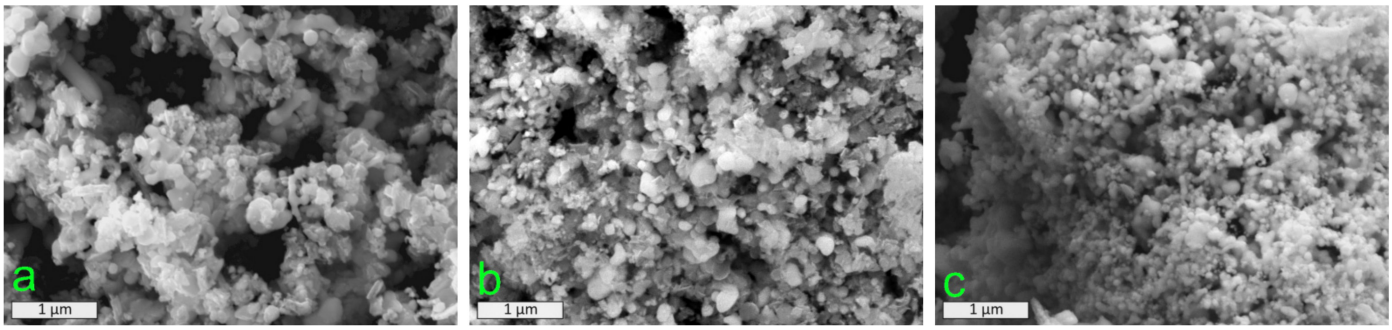


Figure 2. SEM micrographs of the submicrometric powders synthesized by SHS (×20,000). (**a**) W-2 wt.% Cr (WCr2), (**b**) W-4 wt.% Cr (WCr4), and (**c**) W-6 wt.% Cr (WCr6).

X-ray diffraction patterns of the resulting powders are presented in Figure 3, and the results of the Rietveld analysis performed on these diffraction patterns are summarized in Table 2. In these patterns, the five main peaks come from the diffraction of tungsten, revealing the α, Body Centered Cubic (BCC) crystal structure, as expected. However, specifically, when the reaction chamber is not sealed, some additional peaks are also observed and are the signature of the presence of WO_3 and WO_2, which remain despite the excess Mg used. These residual tungsten oxide peaks are significant for the WCr2 sample synthesized without confinement and much less, but still clearly visible when

confinement was used. Indeed, the reaction temperature is ~700 °C above the boiling point of magnesium, and, despite using a sealed reactor, this magnesium might escape away from the reaction zone and condense on the salt surrounding the sample, yielding an incompletely converted reaction product. However, we have shown that when increasing the size of the sample, the amount of oxidized tungsten present in the final powder decreases [45]. Nevertheless, it seems that the total amount of residual oxide phases decreases when the Cr amount is increased. Although the presence of chromium inside the alloy was intended to increase its oxidation resistance, it is unlikely that the residual oxides observed on WCr2 and WCr4 result from oxidation of the nanopowders; indeed, although this oxidation most likely takes place during air exposure, it should produce amorphous oxides, which would be undetected by XRD. We rather suspect that the presence of Cr_2O_3 together with WO_3 modifies the reaction kinetics and improves its final yield. Finally, there is a distinct shift of the diffraction peaks when the Cr amount is increased, which could be attributed to a greater amount of Cr within the W lattice, as the Cr lattice is smaller than the one for W. Moreover, an imperfect mixing of the two elements is suspected for WCr4 and WCr6, as distinct shoulders are visible to the right of the peaks (Figure 3b).

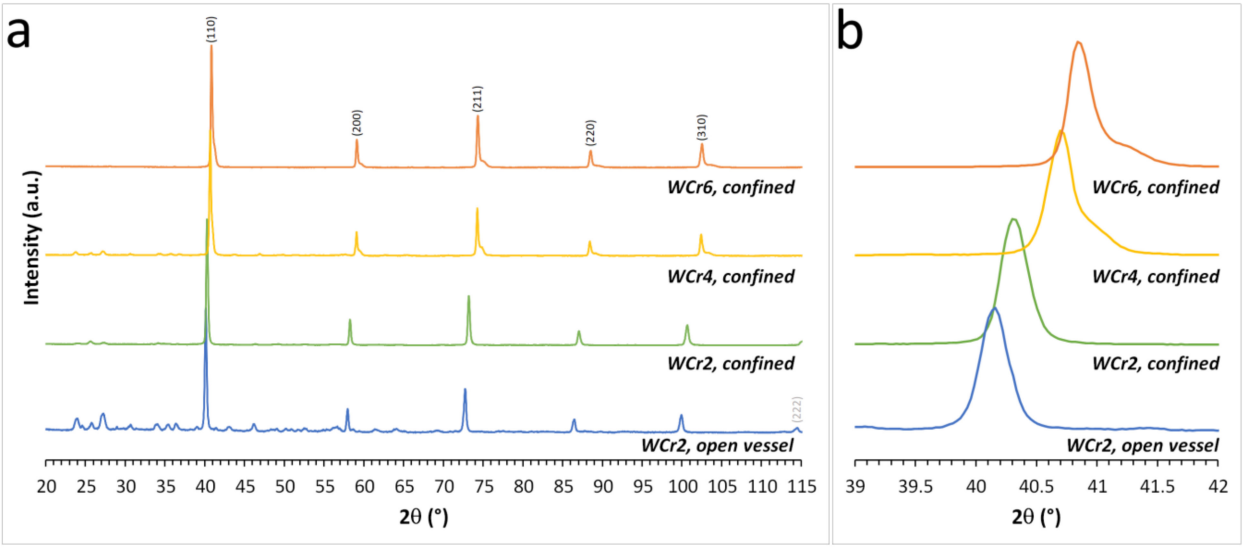


Figure 3. (**a**) X-ray diffraction pattern of the powders after synthesis, lixiviation, rinsing and drying. Miller indices represented correspond to the expected tungsten BCC crystal structure. The other peaks observed on the XRD patterns are attributed to tungsten oxides WO_3 and WO_2. (**b**) Magnification of the (110) peak.

Table 2. Rietveld refinement of powders XRD patterns. Results shown correspond to the main BCC phase only.

Alloy	Lattice Parameter (nm)
WCr2, open vessel	0.31814
WCr2, confined	0.31642
WCr4, confined	0.31241
WCr6, confined	0.31220

3.2. SPS Densification

For the sake of clarity, as no significant differences are observed between the different cycles, we will present here the results concerning the 3 different alloys compacted at 1800 °C, Figure 4. As the mass and thicknesses of the three samples are different, the curves representing the kinetics of densification dz/dt are normalized, so their integrals are equal to 1.

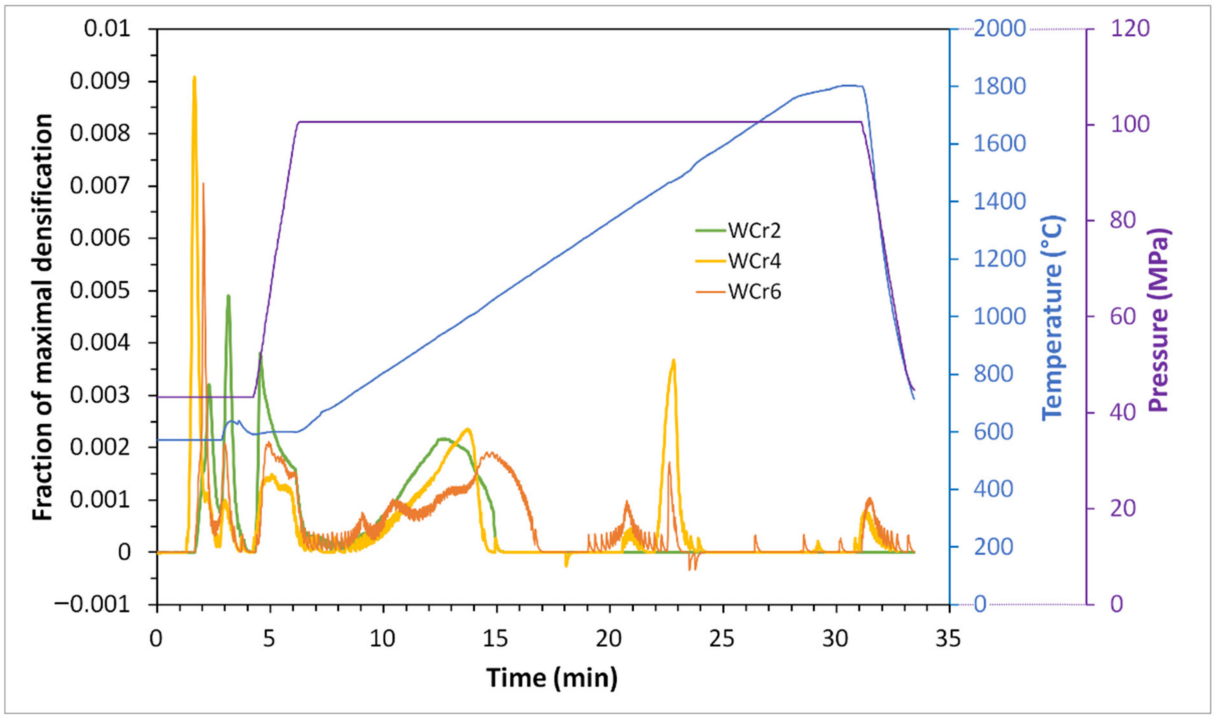


Figure 4. Spark plasma sintering (SPS) cycle (1800 °C—1′). Purple: pressure; blue: temperature; and green, yellow and orange: kinetics of densification as a fraction of total densification (integral of each curve is equal to 1).

A first densification peak is observed at low-temperature, below the lower pyrometer limit at 600 °C, and is due to outgassing, possibly of residual water if the drying step was incomplete. From 4 to 6.5 min, while the temperature is constant just above the detection limit of the pyrometer, the pressure on the sample is increased, and a second densification peak is observed on all three samples. After this first step, densification stops temporarily and then resumes progressively as the temperature is increased, with maximal densification kinetic at 12.4, 13.6 and 14.8 min for WCr2, WCr4 and WCr6, respectively (with corresponding temperatures of 930, 995 and 1055 °C, respectively). These low temperatures thus show the influence of the nanometric grain sizes on the sintering of tungsten. It is worth mentioning that despite chromium has a lower melting temperature, and despite the fact that powders particle sizes decrease with the increasing amount of chromium, the sintering nevertheless arises with increasing temperatures. A third, abrupt peak is observed when the temperature is in the 1465–1475 °C range. As this temperature corresponds to the tungsten trioxide melting temperature (1473 °C), we believe that a liquid phase is then present, and densification may proceed almost freely. No significant evolution in the density can be observed when the temperature is further increased to 1800 °C, nor during the 5 min plateau. Although the WCr2 yielded an incomplete reading of the densification process (saturation of the detector after 15′), it should be noted that the intensity of the shrinkage of the sample decreases when the Cr amount increases at that temperature. Indeed, the WCr6 powders had fewer residual oxides (no crystalized oxides detectable on the XRD pattern, Figure 2) and most certainly less amorphous oxides at the surface of the nanopowders after air exposure due to the Cr-induced passivation of the powders. Finally, at the end of the cycle, the temperature is abruptly decreased, yielding a shrinking of the sample due to natural thermal expansion, and an apparent densification step is observed.

A temperature of 1600 °C seems therefore sufficient to fully densify the W nanopowders produced. However, due to the melting of the oxides at or around 1473 °C, and their subsequent flowing outside of the sample, a small mass loss was observed. It is, however,

considerably smaller than what had been observed when pure tungsten samples were sintered [46].

3.3. Densified Samples

Measured densities using Archimedes' method were greater than 90% of the theoretical density for all samples and up to 99.91% (Table 3). Comparatively to previously published results, these densities extremely promising: Yao et al. [48] studied the densification of commercial 50 nm tungsten nanometer at a similar temperature, only limiting the pressure to 50 MPa, for a final relative density of 97.8%, and, to obtain a density of 99%, similar to the results presented here, the use of resistance sintering under ultra high-pressure (RSUHP) at 9 GPa was necessary. Comparatively, the densification of micrometric commercial tungsten powder (2 µm) using SPS could only provide a density of 84.3% (50 MPa, 1600 °C) [18], and 92.16% using hot pressing (1800 °C, 2 h, 20 MPa) [49]. The specific granulometry and its polydispersity, the specific shape of the initial powder grains seem, therefore, very favorable to the densification.

Table 3. Relative density, Vickers hardness and Rietveld refinement results on SPS-densified samples. In bulk are the samples described more specifically in the text.

Alloy	Sintering Temperature (°C)	Plateau Duration (min)	Relative Density (%)	Vickers Hardness	Lattice Parameter (nm)	Crystallite Size (nm)
WCr2	1600	1	90.86	335.7	0.31645	75.9
WCr2	1800	1	98.10	314.8	0.31672	68.4
WCr4	1800	1	99.91	349.7	0.31682	68.5
WCr4	1800	5	99.78	244.1	0.31669	78.0
WCr4	2000	15	98.85	264.5	0.31666	78.3
WCr6	1800	1	99.12	420.6	0.31676	79.6

Bulk samples were analyzed using X-ray diffraction, Figure 5, then by Rietveld refinement, Figure 5 presents the X-ray diffraction patterns obtained on densified samples, and Table 3 summarizes the results of the Rietveld analysis. These diffraction patterns only display the characteristic peaks of the tungsten BCC crystal structure, and no residual (crystalized) oxide phases can be detected, accordingly to the hypothesis formulated when analyzing densification curves, attributing the third densification peak at 1473 °C to the melting of the tungsten oxides and their subsequent flowing outside of the sample. This, unfortunately, implies a small mass loss, although significantly lower than what was observed on pure W [46], but raises the possibility of obtaining pure nanostructured bulk tungsten alloys.

Contrary to what could be expected from the XRD analysis performed previously on the powders, no peak shift is observed on the different samples, and the calculated lattice parameters are very similar. Moreover, crystallites sizes are comparable, in the 68–80 nm range, despite a significant difference observed on the powder SEM images. To analyze further these diffraction patterns, we performed a magnification of the (211) peak. Whereas the positions of this peak do not seem to shift significantly, its asymmetry seems to slightly vary with the composition due to the presence of different compositional gradients as a function of the Cr content, which Rietveld analysis seems to not take correctly into account. However, this seems strongly insufficient to explain the variation of the lattice parameters from the powders to the bulk samples. As backscattered images of the three samples (not presented) show a strong increase of the Cr-rich phase (in black on Figure 6) with the Cr content, a Cr depletion cannot be the cause of the newly gained homogeneity of the lattice parameters. On the contrary, we suspect that the strong shift observed on the powders do not provide only from the addition of Cr but also from some unaccounted form of out-of-equilibria state of these powders, which disappears after densification.

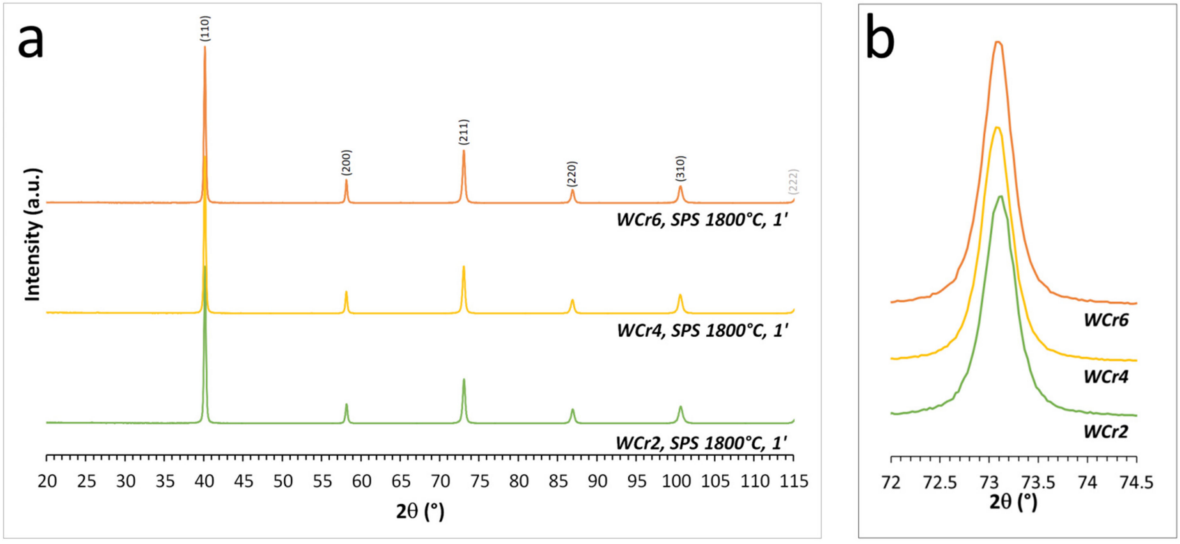


Figure 5. (**a**) XRD patterns of SPS sintered samples. Miller indices represented correspond to the expected tungsten BCC crystal structure. (**b**) magnification of the (211) peak.

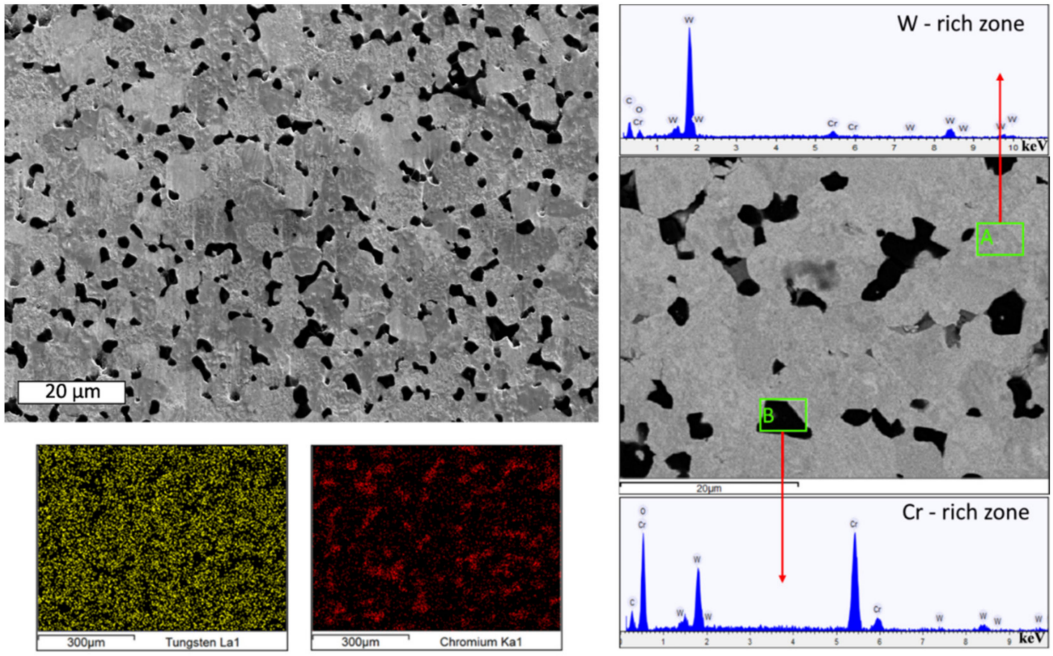


Figure 6. Upper left: SEM observation of the WCr6 sintered sample (2000 °C—5′). Right: EDX analysis of W-rich and Cr-rich regions; bottom left: EDX mapping on a large-scale of the sample.

Figure 6 shows an SEM observation of the WCr6 samples sintered at 2000 °C for 5′. On this image, the microstructure of the densified samples seems to be within a grain size range of 5 to 10 µm, and this apparent crystal growth seems more pronounced for higher W contents. Moreover, when the Cr content is 4 or 6 wt.%, dark areas appear and are naturally in greater proportions for WCr6 than for WCr4.

EDS local analysis and mapping of the sample proved these regions to also be a W-Cr alloy but significantly richer in Cr than the average of the sample. However, when performing EBSD analysis to study this apparent loss of the nanostructure, Figure 7, these micrometric grains turn out to be, for the most part, nanostructured or with a high concentration of low-angle grain boundaries (LAGB), with grain sizes consistent to the measured value obtained by Rietveld refinement (Table 3). Surprisingly, the presence

of a real nanosubstructure is the strongest for WCr2 and WCr6 and significantly less pronounced for WCr4. This nanostructuration is also of utmost importance for Plasma Facing Components as several experimental studies on metals [50,51], intermetallics [52], and ceramic materials [53,54] have shown that it would improve irradiation resistance. Dark areas are these images correspond to unresolved Kikuchi line patterns, which could be due to a different crystal structure, e.g., the presence of an oxide, or to a local loss of flatness of the sample such as a grain tear-off during polishing. In order to resolve this issue, Figure 8 presents the same magnified area of the sample observed on EBSD and SEM, where it can clearly be seen that the dark areas observed on the SEM images are properly indexed within the BCC structure, which confirms that they are made of a W-Cr alloy (and are therefore not recrystallized chromium oxide, which crystallizes with the corundum, hexagonal structure). Simultaneously, black, unindexed regions on the EBSD image due to unresolved Kikuchi lines patterns correspond to regions on the SEM image where significant irregularities are observed, seemingly from grain tear-off during polishing. This result is in good agreement with the XRD pattern, where no other phase was detected besides the BCC structure.

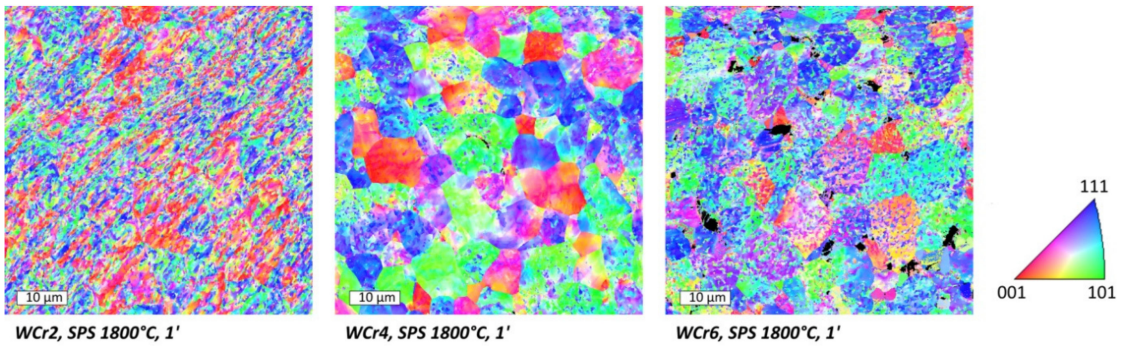


Figure 7. Electron backscattered diffraction (EBSD) images representing the grain orientations on 60 × 60 µm^2 areas.

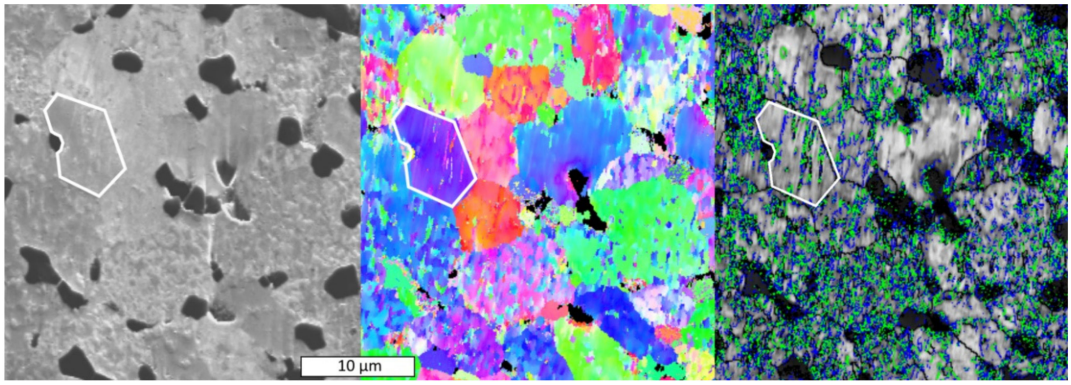


Figure 8. SEM (**left**) and EBSD (**center**) and (**right**) images of the same area, showing the dark SEM areas to be correctly indexed with the BCC structure, and the black EBSD areas to correspond to surface irregularities (marked grain is for the eye's guidance only); the right image shows the positions of the High-Angle Grain Boundaries (HAGB) (in black) and Low-Angle Grain Boundaries (LAGB) (2–5° rotation angle in blue, 5–15° in green).

From the EBSD patterns in Figure 7, it is possible to retrieve the (110), (200) and (211) pole figures as shown for the WCr4 sample in Figure 9. While the symmetry of these patterns is poor, inverse pole figures calculated from these and presented in Figure 10 show a significant trend for the material towards a 111 preferential orientation. However, this analysis is performed on a small, 60 × 60 µm^2 area, and is most certainly not statistically significant. A similar result was obtained on pure W, although in that case, grains were in the form of platelets, and a preferential orientation could be explained from an anisotropic compression behavior of the powders during SPS sintering [46]. It is much harder to

explain the origin of the preferential orientation here, as the powders were, if not spherical, at least mainly rounded (Figure 2), with only a few sharp-edged particles. A more precise analysis on a larger area, e.g., using quantitative texture analysis using XRD, would be necessary to confirm this result, but was unfortunately not performed before the samples were destroyed during mechanical testing.

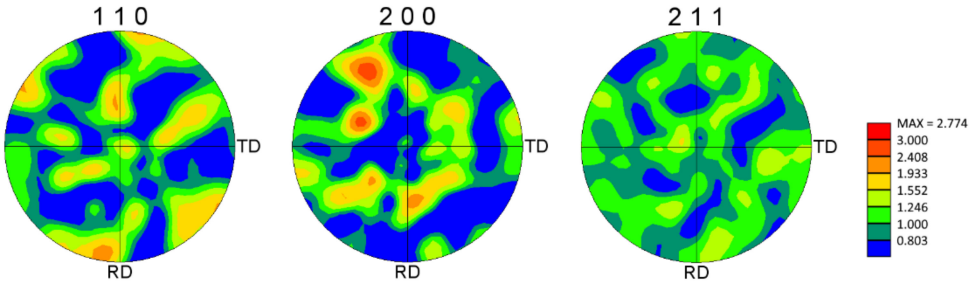


Figure 9. 110, 200 and 211 pole figures calculated from the EBSD mapping of the WCr4 sample presented in Figure 7.

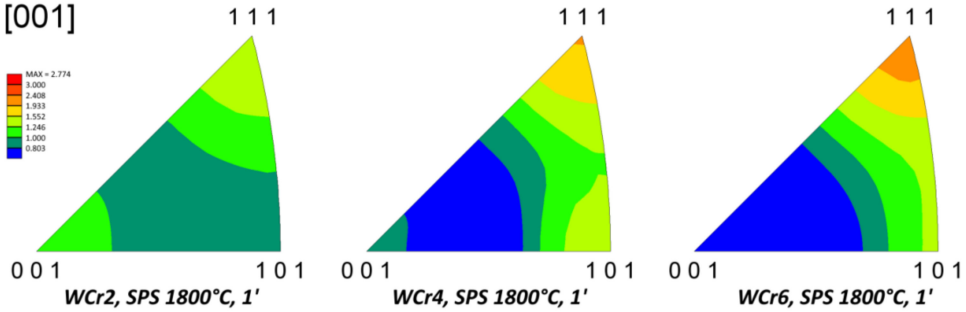


Figure 10. Inverse pole figures calculated from the three EBSD mappings (Figure 7).

Vickers hardness measurements are summarized in Table 3. The theoretical hardness for pure tungsten, as provided in the literature, is 343 HV, and, as the nanostructuration of a material is known to increase the hardness [48], increased hardnesses were expected for the samples presented here. Moreover, the hardness of 1142 HV was found in the literature for stoichiometric W-Cr alloy [47], adding another reason for an increase in hardness to be expected in our alloys. Indeed, results presented in Table 3 show an increase in hardness related to the composition: the three alloys sintered at 1800 °C for 1′ have hardness values from 315 Hv for WCr2 to 420 Hv for WCr6. In the meantime, comparing the WCr2 samples sintered at 1600 °C and 1800 °C, respectively, a drop in hardness value is observed, as partial recrystallization may occur at high-temperature. A similar result is observed on the WCr4 samples, simply by increasing the plateau duration to 5′. This drop in hardness is, however, limited, and the value measured for the sample sintered at 2000 °C with a plateau duration of 15′ is almost identical to the previous one. It is, however, difficult, in these conditions, to clearly identify if this increase in hardness is due to the presence of an alloying element or to the nanostructuration of the material

Results of compression tests are presented in Figure 11. They depict a ductility at room temperature in the range of 9 to 10%. Apparent mechanical properties deduced from these curves are summarized in Table 4. These results show a slight increase in the elastic limit, compared to pure, micrometric, tungsten, but is still slightly lower than the values obtained with pure, "cold rolled" (at temperatures ranging from 600 °C to 1000 °C) pure tungsten [32]. Indeed, the well-known Hall–Petch effect associates the decrease of the grain sizes to improved mechanical properties, and this result was therefore expected. However, the main improvement concerns the obtained ductility of the resulting materials, as the same study only reached a maximal engineering strain of 3–4% before rupture and <1% before the maximum stress is reached ([34], Figure 2). With values reaching 9–10% for the

strain at the maximum stress and 16–18% strain at failure at room temperature, our results are therefore very promising for the development of new refractory ductile components.

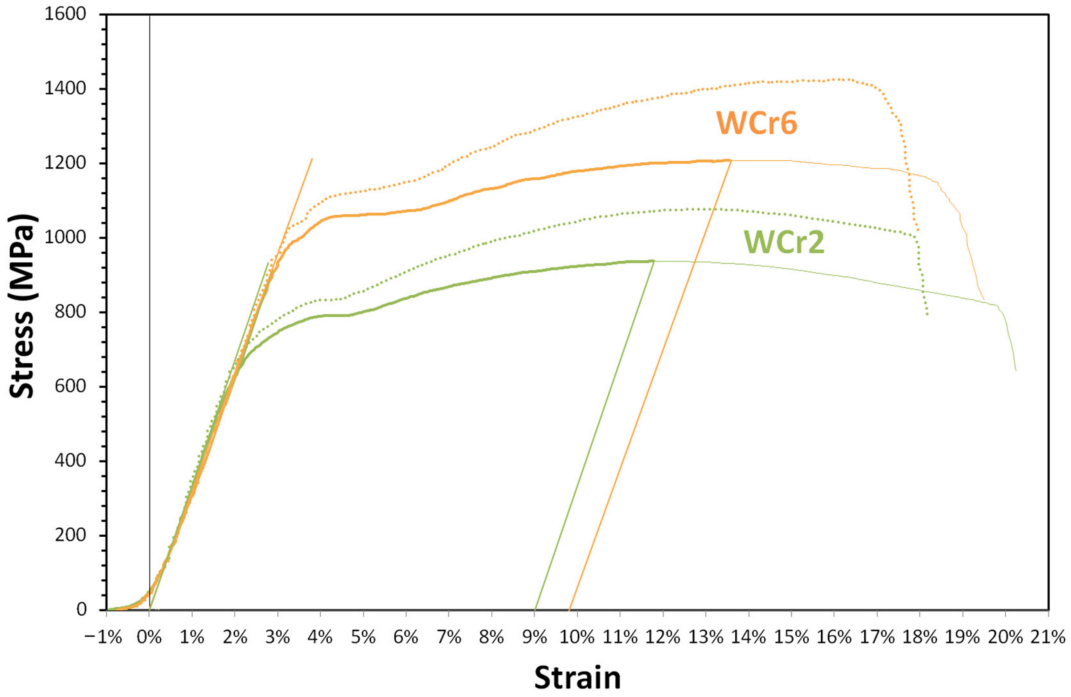


Figure 11. Results from the compression tests. Dotted lines: engineering strain/stress curves; full lines: true stress/strain curves, showing a ductility of 9.00% and 9.74%.

Table 4. Results of compression tests. Ductility is the plastic deformation only at the maximum strength.

Alloy	Elastic Limit (MPa)	Apparent Young's Modulus (GPa)	Yield Strength (MPa)	Ductility (%)
WCr2	600	33.8	937	9.00
WCr6	950	31.6	1208	9.74

4. Conclusions

Magnesio-thermitic reactions were used to synthesize tungsten-chromium alloys with a morphology of nanometric to submicronic powders. Densification was then performed using SPS, with a final density of up to 99.9% of the theoretical value while preserving the nanometric substructure of the grains. Such a microstructure is thought to be favorable to increase resistance to ablation and spallation. On the other hand, the main aim of our effort to obtain this microstructure was to increase mechanical properties, and specifically ductility. Compressive testing of the samples presented an elastic limit ranging from 700 to 1000 MPa, depending on the alloy composition, while displaying a ductility greater than 9%. Future investigations will focus on slightly more complex alloys, with 2–3 alloying elements, in order not only to improve further mechanical properties but also to study the resistance of the materials to recrystallization at high-temperature.

Author Contributions: S.D. was the principal investigator of this study, performed unser the supervision and in collaboration with D.V.; C.G., working with E.B., was the coordinator of a broader topic on Plasma Facing Materials, and brought valuable insight all along this study; N.H. provided clear information and inerpretation of various analyses in this study, expecially SEM. D.T. provided help durind g SPS synthesis and performed EBDS analyses. The paper has been mainly written by D.V. All authors have read and agreed to the published version of the manuscript.

Funding: This research received no external funding.

Data Availability Statement: No significant data in this study were created or analyzed in this study, aside from the one presented here. Additional data are available on request from the corresponding author.

Conflicts of Interest: The authors declare no conflict of interest.

References

1. Joachim, R.; Klaus, S. Hydrogen in tungsten as plasma-facing material. *Phys. Scr.* **2011**, *T145*, 014031.
2. Bolt, H.; Barabash, V.; Krauss, W.; Linke, J.; Neu, R.; Suzuki, S.; Yoshida, N.; Team, A.U. Materials for the plasma-facing components of fusion reactors. *J. Nucl. Mater.* **2004**, *329–333*, 66–73. [CrossRef]
3. Rieth, M.; Boutard, J.L.; Dudarev, S.L.; Ahlgren, T.; Antusch, S.; Baluc, N.; Barthe, M.-F.; Becquart, C.S.; Ciupinskie, L.; Correia, J.B.; et al. Review on the EFDA programme on tungsten materials technology and science. *J. Nucl. Mater.* **2011**, *417*, 463–467. [CrossRef]
4. Zhou, Z.; Ma, Y.; Du, J.; Linke, J. Fabrication and characterization of ultra-fine grained tungsten by resistance sintering under ultra-high pressure. *Mater. Sci. Eng. A* **2009**, *505*, 131–135. [CrossRef]
5. Cottrell, G.A. Sigma phase formation in irradiated tungsten, tantalum and molybdenum in a fusion power plant. *J. Nucl. Mater.* **2004**, *334*, 166–168. [CrossRef]
6. Pintsuk, G. Tungsten as a Plasma-Facing Material, Reference Module in Materials Science and Materials Engineering—Comprehensive. *Nucl. Mater.* **2012**, *4*, 551–581.
7. El-Kharbachi, A.; Chene, J.; Garcia-Argote, S.; Marchetti, L.; Martin, F.; Miserque, F.; Vrel, D.; Redolfi, M.; Malard, V.; Grisolia, C.; et al. Tritium absorption/desorption in ITER-like tungsten particles. *Int. J. Hydrogen Energy* **2014**, *39*, 10525–10536. [CrossRef]
8. Pestchanyi, S.E.; Linke, J. Simulation of cracks in tungsten under ITER specific transient heat loads. *Fusion Eng. Des.* **2007**, *82*, 1657–1663. [CrossRef]
9. Wittlich, K.; Hirai, T.; Compan, J.; Klimov, N.; Linke, J.; Loarte, A.; Merola, M.; Pintsuk, G.; Podkovyrov, V.; Singheiser, L.; et al. Damage structure in divertor armor materials exposed to multiple ITER relevant ELM loads. *Fusion Eng. Des.* **2009**, *84*, 1982–1986. [CrossRef]
10. Mutoh, Y.; Ichikawa, K.; Nagata, K.; Takeuchi, M. Effect of rhenium addition on fracture toughness of tungsten at elevated temperatures. *J. Mater. Sci.* **1995**, *30*, 770–775. [CrossRef]
11. Barabash, V.; Akiba, M.; Mazul, I.; Ulrickson, M.; Vieider, G. Selection, development and charaterisation of plasma facing materials for ITER. *J. Nucl. Mater.* **1996**, *233–237*, 718–723. [CrossRef]
12. El-Guebaly, L.; Kurtz, R.; Rieth, M.; Kurishita, H.; Robinson, A.; Team, A. W-based alloys for advanced divertor designs: Options and environmental impact of state-of-the-art alloys. *Fusion Sci. Technol.* **2011**, *60*, 185–189. [CrossRef]
13. Wurster, S.; Baluc, N.; Battabyal, M.; Crosby, T.; Du, J.; García-Rosales, C.; Hasegawa, A.; Hoffmann, A.; Kimura, A.; Kurishita, H.; et al. Recent progress in R&D on tungsten alloys for divertor structural and plasma facing materials. *J. Nucl. Mater.* **2013**, *442*, S181–S189.
14. Grisolia, C.; Hodille, E.; Chene, J.; Garcia-Argote, S.; Pieters, G.; El-Kharbachi, A.; Marchetti, L.; Martin, F.; Miserque, F.; Vrel, D.; et al. Tritium absorption and desorption in ITER relevant materials: Comparative study of tungsten dust and massive samples. *J. Nucl. Mater.* **2015**, *463*, 885–888. [CrossRef]
15. Coenen, J.W.; Philipps, V.; Brezinsek, S.; Pintsuk, G.; Uytdenhouwen, I.; Wirtz, M.; Kreter, A.; Sugiyama, K.; Kurishita, H.; Torikai, Y.; et al. Melt-layer ejection and material changes of three different tungsten materials under high heat-flux conditions in the tokamak edge plasma of TEXTOR. *Nucl. Fusion* **2011**, *51*, 113020. [CrossRef]
16. Aguirre, M.V.; Martín, A.; Pastor, J.Y.; Llorca, J.; Monge, M.A.; Pareja, R. Mechanical behavior of W-Y_2O_3 and W-Ti alloys from 25 °C to 1000 °C. *Metall. Mater. Trans. A* **2009**, *40*, 2283–2290. [CrossRef]
17. Aguirre, M.V.; Martín, A.; Pastor, J.Y.; Llorca, J.; Monge, M.A.; Pareja, R. Mechanical properties of Y_2O_3-doped W-Ti alloys. *J. Nucl. Mater.* **2010**, *404*, 203–209. [CrossRef]
18. Arshad, K.; Guo, W.; Wang, J.; Zhao, M.Y.; Yuan, Y.; Zhang, Y.; Wang, B.; Zhou, Z.-J.; Lu, G.-H. Influence of vanadium precursor powder size on microstructures and properties of W-V alloy. *Int. J. Refract. Met. Hard Mater.* **2015**, *50*, 59–64. [CrossRef]
19. Arshad, K.; Yuan, Y.; Cheng, L.; Wang, J.; Zhou, Z.J.; De Temmerman, G.; Lu, G.-H. Deuterium blistering in tungsten and tungsten vanadium alloys. *Fusion Eng. Des.* **2016**, *107*, 25–31. [CrossRef]
20. López-Ruiz, P.; Koch, F.; Ordás, N.; Lindig, S.; García-Rosales, C. Manufacturing of self-passivating W-Cr-Si alloys by mechanical alloying and HIP. *Fusion Eng. Des.* **2011**, *86*, 1719–1723. [CrossRef]
21. Telu, S.; Mitra, R.; Pabi, S.K. High temperature oxidation behavior of W–Cr–Nb Alloys in the Temperature Range of 800–1200 °C. *Int. J. Refract. Met. Hard Mater.* **2013**, *38*, 47–59. [CrossRef]
22. Telu, S.; Patra, A.; Sankaranarayana, M.; Mitra, R.; Pabi, S.K. Microstructure and cyclic oxidation behavior of W-Cr alloys prepared by sintering of mechanically alloyed nanocrystalline powders. *Int. J. Refract. Met. Hard Mater.* **2013**, *36*, 191–203. [CrossRef]
23. Zhou, Y.; Sun, Q.X.; Xie, Z.M.; Liu, R.; Wang, X.P.; Fang, Q.F.; Liu, C.S. The microstructure and microhardness of W–5wt% Cr alloy fabricated by spark plasma sintering. *J. Alloys Compd.* **2014**, *585*, 771–775. [CrossRef]

24. Veleva, L.; Oksiuta, Z.; Vogt, U.; Baluc, N. Sintering and characterization of W–Y and W–Y_2O_3 materials. *Fusion Eng. Des.* **2009**, *84*, 1920–1924. [CrossRef]
25. Liu, R.; Xie, Z.M.; Fang, Q.F.; Zhang, T.; Wang, X.P.; Haoa, T.; Liua, C.S.; Daic, Y. Nanostructured yttria dispersion-strengthened tungsten synthesized by sol-gel method. *J. Alloys Compd.* **2016**, *657*, 73–80. [CrossRef]
26. Kurishita, H.; Matsuo, S.; Arakawa, H.; Narui, M.; Yamazaki, M.; Sakamotob, T.; Kobayashib, S.; Nakaib, K.; Takidac, T.; Takebec, K.; et al. High temperature tensile properties and their application to toughness enhancement in ultra-fine grained W-(0-1.5)wt% TiC. *J. Nucl. Mater.* **2009**, *386–388*, 579–582. [CrossRef]
27. Kurishita, H.; Matsuo, S.; Arakawa, H.; Sakamoto, T.; Kobayashi, S.; Nakai, K.; Takida, T.; Kato, M.; Kawai, M.; Yoshida, N. Development of re-crystallized W–1.1%TiC with enhanced room-temperature ductility and radiation performance. *J. Nucl. Mater.* **2010**, *398*, 87–92. [CrossRef]
28. Zhang, T.; Wang, Y.; Zhou, Y.; Song, G. Effect of heat treatment on microstructure and mechanical properties of ZrC particles reinforced tungsten-matrix composites. *Mater. Sci. Eng. A* **2009**, *512*, 19–25. [CrossRef]
29. Hao, T.; Fan, Z.Q.; Zhang, T.; Luo, G.N.; Wang, X.P.; Liu, C.; Fang, Q. Strength and ductility improvement of ultrafine-grained tungsten produced by equal-channel angular pressing. *J. Nucl. Mater.* **2014**, *455*, 595–599. [CrossRef]
30. Levin, Z.S.; Hartwig, K.T. Strong ductile bulk tungsten. *Mater. Sci. Eng. A* **2017**, *707*, 602–611. [CrossRef]
31. Németh, A.A.N.; Reiser, J.; Armstrong, D.E.J.; Rieth, M. The nature of the brittle-to-ductile transition of ultrafine grained tungsten (W) foil. *Int. J. Refract. Met. Hard Mater.* **2015**, *50*, 9–15. [CrossRef]
32. Reiser, J.; Hoffmann, J.; Jäntsch, U.; Klimenkov, M.; Bonk, S.; Bonnekoh, C.; Rieth, M.; Hoffmann, A.; Mrotzek, T. Ductilisation of tungsten (W): On the shift of the brittle-to-ductile transition (BDT) to lower temperatures through cold rolling. *Int. J. Refract. Met. Hard Mater.* **2016**, *54*, 351–369. [CrossRef]
33. Reiser, J.; Hoffmann, J.; Jäntsch, U.; Klimenkov, M.; Bonk, S.; Bonnekoh, C.; Hoffmann, A.; Mrotzek, T.; Rieth, M. Ductilisation of tungsten (W): On the increase of strength AND room-temperature tensile ductility through cold-rolling. *Int. J. Refract. Met. Hard Mater.* **2017**, *64*, 261–278. [CrossRef]
34. Guo, H.Y.; Xia, M.; Wu, Z.T.; Chan, L.C.; Dai, Y.; Wang, K.; Yan, Q.-Z.; He, M.-C.; Ge, C.; Lu, J. Nanocrystalline-grained tungsten prepared by surface mechanical attrition treatment: Microstructure and mechanical properties. *J. Nucl. Mater.* **2016**, *480*, 281–288. [CrossRef]
35. Chen, L.; Ping, L.; Ye, T.; Lingfeng, L.; Kemin, X.; Meng, Z. Observations on the Ductility and Thermostability of Tungsten Processed from Micropowder by Improved High-pressure Torsion. *Rare Met. Mater. Eng.* **2016**, *45*, 3089–3094. [CrossRef]
36. Dzykovich, I.Y.; Panichkina, V.V.; Skorokhod, V.V.; Shaiderman, L.I. Effect of palladium on diffusion processes in the system tungsten-chromium. *Sov. Powder Met. Met. Ceram.* **1976**, *115*, 151–153. [CrossRef]
37. Itagaki, T.; Yoda, R. The Effect of Palladium on Oxidation Behavior of Sintered Tungsten-Chromium-Palladium Alloys. *J. Jpn. Inst. Met.* **1974**, *38*, 486–492. [CrossRef]
38. Zhang, Q.; Zhao, J.C. Impurity and interdiffusion coefficients of the Cr–X (X = Co, Fe, Mo, Nb, Ni, Pd, Pt, Ta) binary systems. *J. Alloys Compd.* **2014**, *604*, 142–150. [CrossRef]
39. Lee, D.B.; Simkovich, G. Oxidation of Mo-W-Cr-Pd alloys. *J. Less Common Met.* **1990**, *163*, 1–62. [CrossRef]
40. Waterstrat, R.M. Analysis of selected alloys in the systems Cr-Pd, Cr-Ru, V-Pd and Ta-Pt. *J. Less Common Met.* **1981**, *80*, P31–P36. [CrossRef]
41. Li, Y.; Li, P.; Bian, H.; Tang, N.; Koizumi, Y.; Chiba, A. The hot forging behaviour and its effects on the oxidation behaviour of W–Cr alloy. *Corros. Sci.* **2014**, *83*, 367–374. [CrossRef]
42. Malewar, R.; Kumar, K.S.; Murty, B.S.; Sarma, B.; Pabi, S.K. On sinterability of nanostructured W produced by high-energy ball milling. *J. Mater. Res.* **2007**, *22*, 1200–1206. [CrossRef]
43. Dine, S.; Aïd, S.; Ouaras, K.; Malard, V.; Odorico, M.; Herlin-Boime, N.; Habert, A.; Gerbil-Margueron, A.; Grisolia, C.; Chêne, J.; et al. Synthesis of tungsten nanopowders: Comparison of milling, SHS, MASHS and milling-induced chemical processes. *Adv. Powder Technol.* **2015**, *26*, 1300–1305. [CrossRef]
44. Kentheswaran, V.; Dine, S.; Vrel, D.; Couzinié, J.P.; Dirras, G. Synthesis of nanometric refractory alloys powders in the MoNbW system. *J. Alloys Compd.* **2016**, *679*, 80–87. [CrossRef]
45. Dine, S.; Kentheswaran, V.; Vrel, D.; Couzinié, J.P.; Dirras, G. Synthesis of nanometric MoNbW alloy using self-propagating high-temperature synthesis. *Adv. Powder Technol.* **2017**, *28*, 1739–1744. [CrossRef]
46. Dine, S.; Bernard, E.; Herlin, N.; Grisolia, C.; Tingaud, D.; Vrel, D. SHS synthesis, SPS densification and mechanical properties of nanometric tungsten. *Adv. Eng. Mater.* **2018**. [CrossRef]
47. Liu, G.; Li, J.; Chen, K.; He, G.; Yang, Z.; Guo, S. High-gravity combustion synthesis of W-Cr alloys with improved hardness. *Mater. Chem. Phys.* **2016**, *182*, 6–9. [CrossRef]
48. Yao, M.; Zhangjian, Z.; Jun, T.; Ming, L. Fabrication of Ultra-fine Grain Tungsten by Combining Spark Plasma Sintering with Resistance Sintering under Ultra High Pressure. *Rare Met. Mater. Eng.* **2011**, *40*, 0004–0008. [CrossRef]
49. Guo, W.; Arshad, K.; Yuan, Y.; Zhao, M.Y.; Shu, X.L.; Zhou, Z.-J.; Zhang, Y.; Lu, G.-H. Effects of vanadium alloying on the microstructures and mechanical properties of hot-pressed tungsten material. *Mod. Phys. Lett. B* **2016**, *30*, 1650216. [CrossRef]
50. Wurster, S.; Pippan, R. Nanostructured metals under irradiation. *Scr. Mater.* **2009**, *60*, 1083–1087. [CrossRef]
51. Nita, N.; Schaeublin, R.; Victoria, M. Impact of irradiation on the microstructure of nanocrystalline materials. *J. Nucl. Mater.* **2004**, *329–333*, 953–957. [CrossRef]

52. Kilmametov, A.R.; Gunderov, D.V.; Valiev, R.Z.; Balogh, A.G.; Hahn, H. Enhanced ion irradiation resistance of bulk nanocrystalline TiNi alloy. *Scr. Mater.* **2008**, *59*, 1027–1030. [CrossRef]
53. Shen, T.D.; Feng, S.; Tang, M.; Valdez, J.A.; Wang, Y.; Sickafus, K.E. Enhanced radiation tolerance in nanocrystalline $MgGa_2O_4$. *Appl. Phys. Lett.* **2007**, *90*, 263115. [CrossRef]
54. Yang, T.; Huang, X.; Wang, C.; Zhang, Y.; Xue, J.; Yan, S.; Wang, Y. Enhanced structural stability of nanoporous zirconia under irradiation of He. *J. Nucl. Mater.* **2012**, *427*, 225–232. [CrossRef]

© 2021. This work is licensed under http://creativecommons.org/licenses/by/3.0/ (the “License”). Notwithstanding the ProQuest Terms and Conditions, you may use this content in accordance with the terms of the License.